Quantification of Oxygen Metabolic Rates in Human Brain With Dynamic ^{17}O MRI: Profile Likelihood Analysis

Dmitry Kurzhunov,[1,2]* Robert Borowiak,[1,2,3,4] Helge Hass,[5] Philipp Wagner,[1,2] Axel Joachim Krafft,[1,2,3,4] Jens Timmer,[5,6]† and Michael Bock[1,2]†

Purpose: Parameter identifiability and confidence intervals were determined using a profile likelihood (PL) analysis method in a quantification model of the cerebral metabolic rate of oxygen consumption ($CMRO_2$) with direct ^{17}O MRI.

Methods: Three-dimensional dynamic ^{17}O MRI datasets of the human brain were acquired after inhalation of $^{17}O_2$ gas with the help of a rebreathing system, and $CMRO_2$ was quantified with a pharmacokinetic model. To analyze the influence of the different model parameters on the identifiability of $CMRO_2$, PLs were calculated for different settings of the model parameters. In particular, the ^{17}O enrichment fraction of the inhaled $^{17}O_2$ gas, α, was investigated assuming a constant and a linearly varying model. Identifiability was analyzed for white and gray matter, and the dependency on different priors was studied.

Results: Prior knowledge about only one α-related parameter was sufficient to resolve the $CMRO_2$ nonidentifiability, and $CMRO_2$ rates (0.72–0.99 μmol/g$_{tissue}$/min in white matter, 1.02–1.78 μmol/g$_{tissue}$/min in gray matter) are in a good agreement with the results of ^{15}O positron emission tomography studies. Nonconstant α values significantly improved model fitting.

Conclusion: The profile likelihood analysis shows that $CMRO_2$ can be measured reliably in ^{17}O gas MRI experiment if the ^{17}O enrichment fraction is used as prior information for the model calculations. **Magn Reson Med 78:1157–1167, 2017. © 2016 International Society for Magnetic Resonance in Medicine.**

Key words: oxygen metabolism; cerebral metabolic rate of oxygen consumption ($CMRO_2$); direct ^{17}O MRI; non-proton MRI; profile likelihood; identifiability analysis

INTRODUCTION

The oxygen metabolism is altered by many neurodegenerative diseases such as Alzheimer's disease, Parkinson's disease, and Huntington's disease (1–9), or in brain tumors (10–14). For a quantitative analysis of the metabolism of these diseases, an imaging method would be desirable that can map the local cerebral metabolic rate of oxygen consumption ($CMRO_2$). The only clinically established method for direct oxygen quantification is positron emission tomography (PET) with the oxygen isotope ^{15}O (3,4,10,15–18); however, it is rarely used due to the short isotope half-life of only 2 min, which requires costly on-site production. As an alternative, many indirect methods for $CMRO_2$ imaging with ^{1}H MRI have been proposed (19–25). Yet, the detection of the MR accessible stable oxygen isotope ^{17}O is preferable for $CMRO_2$ quantification as it can directly detect the metabolic end product $H_2{}^{17}$O. To calculate metabolic rates of oxygen consumption in humans, the ^{17}O MRI signal changes from $H_2{}^{17}$O molecules are observed during and after inhalation of isotope-enriched ^{17}O gas (26–33).

Direct ^{17}O MRI and MR spectroscopy has been predominantly performed at ultra-high magnetic fields (UHFs) of 7T and 9.4T (26–29,32–36). UHFs are advantageous for ^{17}O MRI because they partly compensate for the low MR sensitivity of the ^{17}O isotope which is only about $1.1 \cdot 10^{-5}$ of ^{1}H due to the low natural abundance of ^{17}O nucleus of 0.037% and the approximately sevenfold lower gyromagnetic ratio. Unfortunately, UHF MR systems are not widely available and are not yet used in clinical routine. Recently, feasibility of direct ^{17}O MRI in human brain and heart at clinical field strengths of 3T has been reported (37), which has the ultimate goal of implementing $CMRO_2$ quantification at clinical MR systems. In the previous studies, a rebreathing (RB) system was implemented for efficient usage of rare and expensive $^{17}O_2$ gas by re-inhalation of the stored $^{17}O_2$ gas in subsequent inhalation cycles (27,33). Unfortunately, this delivery method leads to uncertainties in the determination of the ^{17}O enrichment fraction of the inhaled gas, which in turn can lead to systematic errors in the quantities derived from this enrichment fraction.

Our objective was to exploit the method of profile likelihood (PL) to determine parameter identifiability and their confidence intervals (CIs) in a nonlinear $CMRO_2$ quantification model. Using a recently proposed mathematical modeling framework (38), likelihood-based CIs are considered instead of CIs based on Fisher information which cannot be applied for nonlinear $CMRO_2$ quantification models with sparsely sampled ^{17}O signal-time curves (39). The likelihood-based CI for a parameter is determined by scanning the particular parameter along

[1]Department of Radiology, Medical Physics, University Medical Center Freiburg, Freiburg, Germany.

[2]Faculty of Medicine, University of Freiburg, Freiburg, Germany.

[3]German Cancer Consortium, Heidelberg, Germany.

[4]German Cancer Research Center, Heidelberg, Germany.

[5]Institute of Physics, University of Freiburg, Freiburg, Germany.

[6]BIOSS Centre for Biological Signalling Studies, University of Freiburg, Freiburg, Germany.

*Correspondence to: Dmitry Kurzhunov, Department of Radiology, Medical Physics, University Medical Center Freiburg, Breisacher Straße 60a, Freiburg 79106, Germany. E-mail: dmitry.kurzhunov@uniklinik-freiburg.de

†These authors contributed equally to this work.

its axis while reoptimizing all other parameters in the model (see below for a detailed description), thereby revealing nonlinear relations between parameters. Unlike Fisher-based CIs, a parameter profile can become flat as the parameter is driven to its boundaries, indicating that the model structure has to be altered or that additional measurements are required. The parameter is identifiable if the likelihood-based CI is finite. If the CI is infinitely extended in one or two directions, the parameter is practically or structurally non-identifiable, respectively.

Because the proposed modeling framework does not require an analytical solution of differential equations for the $CMRO_2$ rates, more complex input functions can be used for the ^{17}O enrichment fraction. Based on the parameter profiles of the amended pharmacokinetic model, the amount of prior information is analyzed that is crucial for the identifiability of the $CMRO_2$. In addition, the dependence of the $CMRO_2$ uncertainty on the confidence of the prior information is calculated.

THEORY

The temporal behavior of the $H_2^{17}O$ concentration $x(t)$ in the ^{17}O MRI inhalation experiment can be described by the underlying ordinary differential equation (ODE):

$$\dot{x}\Big(t, u(t), \theta\Big) = f\Big(x(t), u(t), \theta\Big), \quad [1]$$

which depends on initial values and kinetic rate parameters contained in θ and an externally provided stimulus $u(t)$. The model components are linked to the measured magnitude of the ^{17}O MR signal, here denoted $y(t)$, by an observational function g:

$$y(t) = g\Big(x\Big(t, u(t), \theta\Big)\Big) + \epsilon(t), \quad [2]$$

with the assumption of Gaussian errors $\epsilon \sim N(0, \sigma^2)$, which is valid if the signal-to-noise ratio (SNR) of the MR images satisfies at least $SNR > 2$ (40). To compare the model response to the measured data, the scaled log-likelihood is calculated via

$$-2\log(\mathfrak{L}) = \chi^2(\theta) = \sum_i \left(\frac{y_i - g\Big(x\Big(t_i, u(t_i), \theta\Big)\Big)}{\sigma_i} \right)^2 + const.$$

$$[3]$$

The optimal parameter set $\hat{\theta}$ is estimated through minimization of $\chi^2(\theta)$. To estimate parameter uncertainties, the PL approach is used (41,42). Herein, the PL of parameter θ_j is defined as

$$PL(\theta_j) = \min_{\theta_{i \neq j}} \chi^2(\theta). \quad [4]$$

The CI of parameter θ_j is then given by all parameter values for which the corresponding likelihood value does not exceed the threshold denoted by Δ_{CL}, the χ^2 distribution with one degree of freedom and confidence level CL (42):

$$CI_{\theta_j, CL} = \{\theta_j | PL(\theta_j) \le \chi^2(\hat{\theta}) + \Delta_{CL}\}. \quad [5]$$

From the CI, fundamental information about the identifiability of parameters can be derived and results in an infinite CI. A flat parameter profile renders the particular parameter as structurally non-identifiable. In this case,

either no information about the parameter is contained in the measurements, or the other parameters can fully compensate if the parameter value is fixed. On the other hand, a parameter profile which exceeds the threshold given by Δ_{CL} in maximal one direction renders the parameter practically non-identifiable (41). Here, the data possess insufficient information to restrict the parameter to a finite CI. Whereas structural non-identifiabilities can be resolved by fixing model parameters, e.g. through prior knowledge, elimination of practical nonidentifiabilities requires additional information through new experiments.

Once the quantification model is modified, the improvement over the original model needs to be determined. For this, the statistical significance of the model change is quantified by the likelihood ratio (LR) test (43). Therein, a null hypothesis H_0: θ_0 is compared with an alternative hypothesis H_1: θ_1, with $\theta_0 \in \theta_1$. As the negative log-likelihood in Equation [3] is minimized, the LR is transformed into differences of χ^2 values. The test statistic reads

$$LR = \chi^2(\hat{\theta_0}) - \chi^2(\hat{\theta_1}). \quad [6]$$

Similar to parameter profiles, the test statistic is asymptotically χ^2-distributed (44) with n_{dof} degrees of freedom according to the difference in dimensionality of both parameter sets: $n_{dof} = n_{\theta_1} - n_{\theta_0}$. Based on $\chi^2_{n_{dof}}$, a P value can be assigned, and the new model is rated an improvement over the original one if $P < 0.05$.

METHODS

^{17}O MRI Measurement

^{17}O MRI data sets from one volunteer were acquired in two dynamic $^{17}O_2$ inhalation experiments (Exp1 and Exp2) on a clinical 3T MR system (Magneton TIM Trio; Siemens Healthcare, Erlangen, Germany) with a custom-built Tx/Rx ^{17}O volume head coil. This four-leg low-pass birdcage coil was tuned to the ^{17}O resonance at $f_0 = 16.7$ MHz and was driven in a linear mode as described previously (30). For dynamic data acquisition, a three-dimensional (3D) ultra-short echo time density-adapted radial acquisition technique (45) was employed, with a nominal spatial resolution Δx of 10 mm (Exp1) and 8 mm (Exp2) at a temporal resolution of 1 min ($T_{pulse} = 0.8$ ms; repetition time = 8/7 ms; echo time = 0.52 ms; bandwidth = 150/175 Hz/pixel; 1 average; 7500/8570 projections × 128 sampling points per projection; readout time = 6.7/5.7 ms). ^{17}O MR images were reconstructed using Kaiser-Bessel gridding (46) without additional filtering of the raw data.

The volunteer inhaled 2.7 L (Exp1) and 2.5 L (Exp2) of 70%-enriched $^{17}O_2$ gas (NUKEM Isotopes Imaging, Alzenau, Germany) via an oxygen gas delivery system with a RB circuit. Gas was administered in pulses of 40/50 mL using a non-MR safe demand oxygen delivery system (DODS) (Oxytron3; Weinmann, Hamburg, Germany), which efficiently delivers the rare and costly $^{17}O_2$ gas to the alveoli by inspirational triggering.

The imaging experiment was divided into a baseline phase (10.5/9.2 min), wherein ^{17}O MR signal was acquired
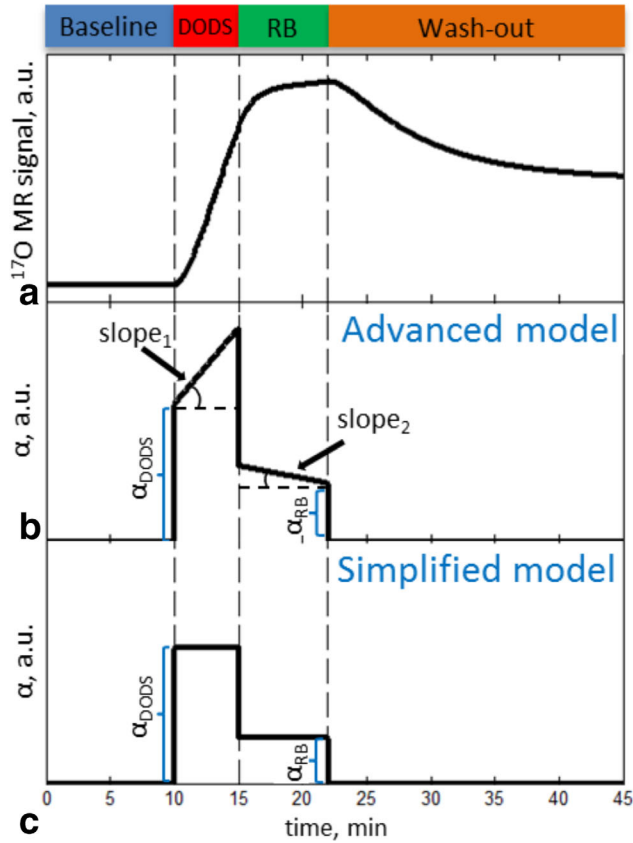
FIG. 1. (**a**) Expected ^{17}O signal change during MR examination with inhalation of $^{17}O_2$ gas based on the reaction rates reported by Hoffmann (33) for WM region. Four phases of the experiment are indicated. (**b**) Time evolution of the ^{17}O enrichment fraction (α) for the advanced CMRO₂ quantification model. It assumes a non-constant enrichment fraction and includes contributions from DODS pulses (α_{DODS}) and $^{17}O_2$ gas stored in the RB circuit, which is described during the DODS phase by s_1 and during the RB phase by α_{RB} and s_2. (**c**) Simplified quantification model, which assumes constant α values.

at natural abundance, followed by two phases with a closed RB system (Fig. 1a): the DODS phase (5/4.2 min), wherein ^{17}O-enriched gas was delivered in pulses, and the RB phase (7.5/5.5 min), during which the volunteer was breathing the gas stored in the RB system (which contains the exhaled $^{17}O_2$ gas that is then reused to increase the ^{17}O MR signal). In the final washout phase (25.1/22 min), the breathing system was opened and the volunteer was breathing room air.

Spatial Registration and Extraction of the ^{17}O Signal-Time Curves

For anatomical comparison and co-registration, a T₁-weighted 3D ^1H MR image was acquired in a separate measurement with a standard MPRAGE sequence (repetition time = 2300 ms; echo time = 2.86 ms; inversion time = 1100 ms; resolution = 0.6 × 0.6 × 1 mm³). First, both ^{17}O and ^1H MR images were interpolated onto 128 × 128 × 128 matrices. The ^1H data were then manually co-registered to the ^{17}O image, which was averaged over the whole MR examination, using anatomical

landmarks that are visible in both images (e.g., the eyes, the ventricles, and the outer contour of the brain) to compensate for the different head positions in the ^1H and the ^{17}O coils. Rigid transformation consisting of translation and rotation in three directions was performed and a transformation matrix for ^1H images was obtained. Second, the software tool Statistical Parametric Mapping Package (SPM8) (47,48) was used to segment gray matter (GM) and white matter (WM) brain regions in the original ^1H MPRAGE data of high spatial resolution. After this, the transformation matrix was applied to the 3D binary masks of WM and GM regions, the masks were then applied to the coregistered ^{17}O MR images. Finally, averaged ^{17}O MR signals were calculated for each tissue to obtain tissue-specific ^{17}O signal-time curves. Partial volume effects were not corrected in this study.

CMRO₂ Quantification Model

In the dynamic ^{17}O MRI experiment, the time evolution of the ^{17}O MR signal is observed. It can be assumed to be linearly correlated with the concentration of ^{17}O due to the short relaxation times (26,37,49). ^{17}O MRI only detects the $H_2{}^{17}O$ signal, and not the $^{17}O_2$ molecules bound to hemoglobin in the blood or in the gas phase (28). Thus, the observed ^{17}O MR signal increase after gas inhalation is exclusively proportional to the amount of the metabolized $H_2{}^{17}O$ water and the time evolution of the measured observable $y(t)$ (Eq. [2]) can be considered to be proportional to the moles of $H_2{}^{17}O$ water $M^{H_2{}^{17}O}$. To convert the ^{17}O MR signal into in vivo $H_2{}^{17}O$ concentration in μmol per gram tissue, the ^{17}O signal intensities before gas inhalation (i.e., during the baseline phase) were normalized using the $H_2{}^{17}O$ natural abundance of 20.56 μmol/g$_{water}$, water partition coefficients [0.71 g/mL for WM and 0.83 g/mL for GM (50)], and averaged density of brain tissue of 1.038 g/mL (51).

Following the principle of mass conservation, the change of the $H_2{}^{17}O$ concentration within a given volume can be caused either by water creation and conversion to other intermediates in the volume, or inward and outward diffusion to or from neighboring volumes. Therefore, the CMRO₂ quantification model, as proposed by Atkinson and Thulborn (26), describes the change $\frac{d}{dt}M^{H_2{}^{17}O}(t)$ in the given volume as an ODE:

$$\frac{d}{dt}M^{H_2{}^{17}O}(t)$$
$$= \underbrace{2 \cdot CMRO_2 \cdot A^{17O}(t)}_{H_2{}^{17}O \ metabolism} - \underbrace{K_L \cdot M^{H_2{}^{17}O}(t)}_{H_2{}^{17}O \ loss} + \underbrace{K_G \cdot B^{H_2{}^{17}O}(t)}_{H_2{}^{17}O \ gain}, \quad [7]$$

where the rate constant K_L reflects the loss by diffusion to blood and chemical conversion to other intermediates and K_G represents the gain by diffusion from blood. A factor of 2 is included because 2 mol of water are produced from one mole of oxygen. $A^{17O}(t)$ denotes the fraction of ^{17}O-labeled arterial oxygen gas with

$$\frac{d}{dt}A^{17O}(t) = \begin{cases} 0 & t < T_{DODS} \\ \rho\left(\alpha - A^{17O}(t)\right) & t > T_{DODS} \end{cases}, \quad [8]$$

and $B^{H_2^{17}O}(t)$ is the relative amount of H$_2$^{17}O in blood (both in excess of natural abundance):

$$\frac{d}{dt}B^{H_2^{17}O}(t) = A^{17}O(t). \qquad [9]$$

Here, α is the ^{17}O enrichment fraction of the inhaled gas above natural abundance, and $\rho = 0.75\,\mathrm{min}^{-1}$ is the rate at which fresh ^{17}O binds to hemoglobin in the pulmonary (26). T_{DODS} denotes the beginning of the ^{17}O gas supply. The expected dynamic signal-time curve $M^{H_2^{17}O}(t)$ in the GM region is shown in Figure 1a based on the rate constants from Hoffmann (33).

Figure 1b shows the proposed time evolution of the enrichment fraction $\alpha(t)$ for the experiment with the RB circuit and a pulsed supply of ^{17}O gas. This curve takes into account that a small fraction of the ^{17}O$_2$ gas is exhaled, as it did not reach the alveoli. Exhaled ^{17}O$_2$ gas is stored in the RB circuit and is used up in subsequent inhalation cycles. Thus, during the DODS phase, in addition to the ^{17}O$_2$ gas being delivered by DODS pulses (α_{DODS}), re-inhalation of the exhaled ^{17}O$_2$ gas occurs, leading to a linear increase in α. Therefore, a linear increasing model with a slope s_1 was introduced. Similarly, in the RB phase, α was assumed to be linearly decreasing (s_2) to α_{RB}. The CMRO$_2$ quantification model can be simplified by setting both slopes s_1 and s_2 to zero (Fig. 1c), i.e. assuming constant α values (26,33), but it might lead to a reduced model fit quality. The advanced model with slopes s_1 and s_2 is hereafter compared with the simplified model with constant α values using the LR test (Eq. [6]).

Model Analysis for CMRO$_2$ Quantification

Parameters of the pharmacokinetic model for CMRO$_2$ quantification were calibrated according to Equation [3]. The numerical optimization was conducted using the trust region-based optimization algorithm *lsqnonlin* implemented in MATLAB (MathWorks, Natick, Massachusetts, USA) (52). In a nonlinear setting, multiple local optima are often present. Thus, a deterministic multistart was performed to find the global optimum (39). All model analysis, optimization and uncertainty calculations were performed within the open-source and freely available MATLAB-based framework D2D (39). Therein, the ODE solver *CVODES* from the SUNDIALS suite is used for ODE integration (53). Following the model calibration, parameter uncertainties of the pharmacokinetic model were calculated. If the target parameter CMRO$_2$ was nonidentifiable, prior information based on estimation of the other model parameters was included to resolve the nonidentifiability. Thereby, a small amount of additional prior information was desired, because the measurement of the models prior is complex and implies additional sources of errors. The influence of the uncertainty of the prior information on the optimal CMRO$_2$ values, estimated through minimization of $\chi^2(\hat{\theta})$ (Eq. [4]), and on the calculated CIs (Eq. [5]) was also investigated. In this case, relative CIs of CMRO$_2$, which are the CIs of CMRO$_2$ divided by the optimal CMRO$_2$ values, were

considered to account for different CMRO$_2$ values in various brain tissues.

To analyze the prediction capability of the advanced pharmacokinetic model for CMRO$_2$, the following approach was taken: first, the model parameters CMRO$_2$, K_L, K_G, α_{DODS}, α_{RB}, s_1, and s_2 were allowed to vary (flat prior) within boundaries of -5 to 3 in log-space. If CMRO$_2$ was non-identifiable, α_{DODS} was fixed to 0.27/0.31 (for Exp1/Exp2) based on the estimated amount of ^{17}O$_2$ inhaled with a single DODS pulse as in (27,32). If CMRO$_2$ was still non-identifiable, an averaged value of α during the DODS phase, which constrains both α_{DODS} and s_1, was used as prior information. This averaged ^{17}O enrichment fraction was calculated based on the total amount of delivered ^{17}O gas and the total duration of DODS phase (0.27/0.31 for Exp1/Exp2). For the simplified pharmacokinetic model, α_{DODS} was fixed to 0.27/0.31 (for Exp1/Exp2). A 10% uncertainty was assumed for both α_{DODS} and the averaged α. Lower and upper boundaries of the CIs of CMRO$_2$, which include the optimum CMRO$_2$ value, were calculated using Equation [5] for the confidence level $CL = 0.33$ and were used to present the calculated CMRO$_2$ values. It is worth noting that in this study the CMRO$_2$ values were presented for each dataset separately, and not as the range among several MR examinations.

RESULTS

An example of a 3D ^{17}O MRI data set with the co-registered ^{1}H MPRAGE image as well as WM and GM masks are shown in Figure 2. The contour of the brain, which has higher water content than the rest of the head, as well as the eyes are clearly visible on ^{17}O MR images. The prototype custom-build coil was driven in the linear mode, which can cause L-R asymmetries in the excitation profile as seen in the posterior parts of the brain due to non-ideal coil matching. These asymmetries, however, have only minor effects on CMRO$_2$ quantification, because H$_2$^{17}O signal-time curves were obtained from large WM and GM regions and were normalized to the baseline before ^{17}O gas inhalation. The number of ^{17}O voxels within the GM region was $59.5 \cdot 10^3$, and $41.0 \cdot 10^3$ within the WM region. The SNR of the MR images acquired within 1 min in the baseline phase were 6/4 for Exp1/Exp2, thus the noise pattern can be assumed to be Gaussian (40), as is presumed in Equation [2].

Figure 3 shows the calculated PLs of the parameters of the advanced CMRO$_2$ quantification model (in log-space), where all model parameters were set with a flat prior, i.e. no prior knowledge about α was assumed. The only quantifiable parameter was K_L, since it determines the decay constant in the wash-out phase, when A^{17}O is zero and B$^{H_2^{17}O}$ is constant (Eq. [7]). The target parameter CMRO$_2$ and the other model parameters were structurally non-identifiable. After assuming a constant value of α_{DODS} (results not shown), CMRO$_2$ still remained non-identifiable.

When the averaged α value during the DODS phase was taken as a constraint, the structural non-identifiability of parameters CMRO$_2$, K_G, and α_{RB} was resolved (Fig. 4). However, either α_{DODS} or s_1 are practically non-identifiable
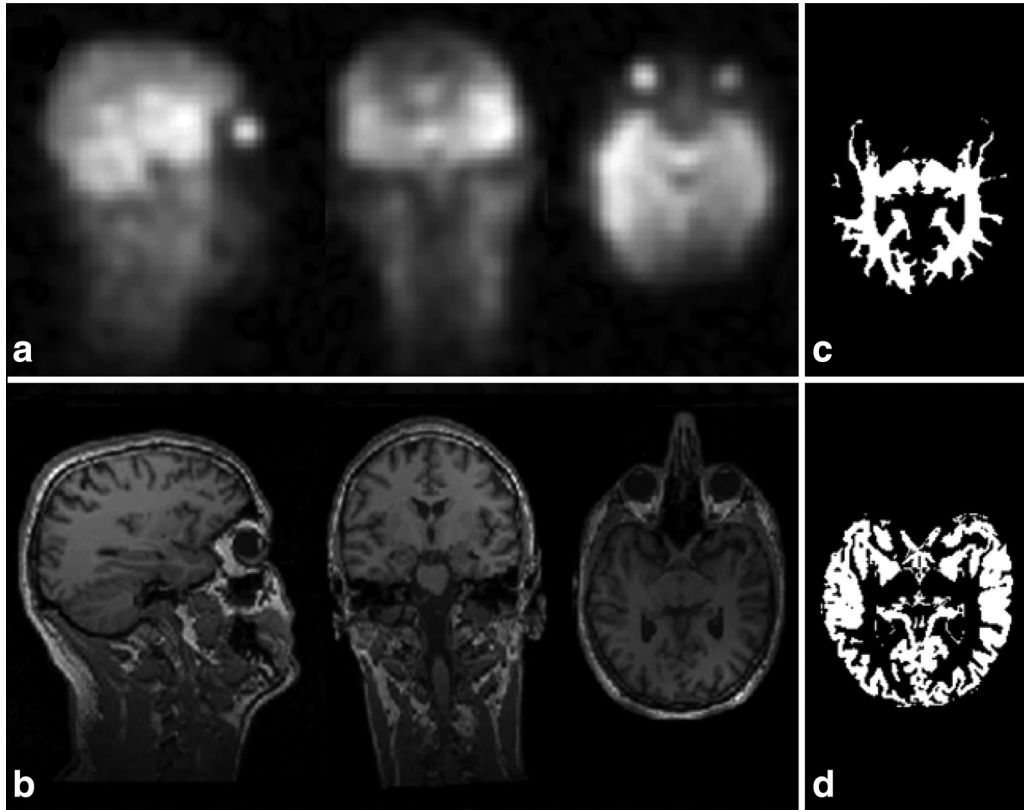
FIG. 2. (**a**) Different orientations of an ¹⁷O MR image from Exp1, averaged over the whole MR examination. (**b**) Coregistered T₁-weighted ¹H MR image. (**c**) Transversal slice of WM mask. (**d**) Transversal slice of GM mask.

for each of the presented data sets. The profile of the parameter s_2 shows that a value of zero (i.e., α is constant during the RB phase) is consistent with the model without impairing the χ^2. The cyan dashed line represents the contribution of the chosen prior to the respective parameter profile. For example, the optimal CMRO₂ value is slightly left from the minimum of the chosen prior, and the CI of the parameters CMRO₂ and K_G are dominated from the uncertainty of the prior. In contrast, the prior uncertainty has a much smaller impact on the CI of K_L and s_2.

Model fits for WM and GM regions are shown in Figure 5, in which prior knowledge about the mean α value during the DODS phase was used. Here, CMRO₂ rates were 0.80–0.99/0.72–0.95 μmol/g$_{tissue}$/min in WM and 1.02–1.27/1.21–1.78 μmol/g$_{tissue}$/min in GM for Exp1/Exp2 (Table 1). Compared with the results of ¹⁵O-PET studies (16), CMRO₂ rates were 34%–42% overestimated in WM and 9%–28% underestimated in GM (Table 1). If one/two of the first DODS pulses are disregarded to account for the 94-mL dead volume of the cable connecting DODS system with nasal cannula (i.e., a later signal onset is assumed), 3%–4%/7%–8% higher CMRO₂ values were found.

In Figure 6, the comparison of model calibration with the advanced and the simplified models is presented. The simplified model shows a stronger deviation from the data in the DODS phase than the advanced model, which is also reflected in the χ^2 values: $\chi^2 = 40.0$ (simplified) and $\chi^2 = 55.6$ (advanced). From this, the LR test, described by

Equation [6], was calculated ($P = 4.1 \cdot 10^{-4} < 0.05$) showing a significant improvement with the advanced model. Moreover, the calculated CMRO₂ in the GM region with the simplified model of 1.11–1.59 μmol/g$_{tissue}$/min is 9% and 18% underestimated compared with the advanced model and with the results of ¹⁵O-PET studies (16).

Figure 7 shows how the α-uncertainty affects the relative CIs of CMRO₂. In this case, CI, which is the difference between upper and lower boundaries of the calculated parameter, represents two standard deviations. These dependences are well represented by a quadratic polynomial, but the CIs are specific for each data set. For example, a 10% uncertainty in α leads to relative CIs of CMRO₂ of 0.22/0.28 for the WM region, and 0.23/0.40 for the GM region in Exp1/Exp2.

DISCUSSION

Altered oxygenation is found in brain tumors and neurodegenerative diseases. Thus, it is of high clinical interest to map oxygen metabolism in clinical routine. With the recent implementation of ¹⁷O MRI (26,27,30–33), clinical CMRO₂ quantification and oxygen metabolism mapping might become feasible; however, the different parameters in the numerical description of the oxygen uptake are often not identifiable from time-resolved measurements alone. In this study, the PL method was used to identify those parameters in the CMRO₂ quantification model that require prior knowledge for a unique identification.
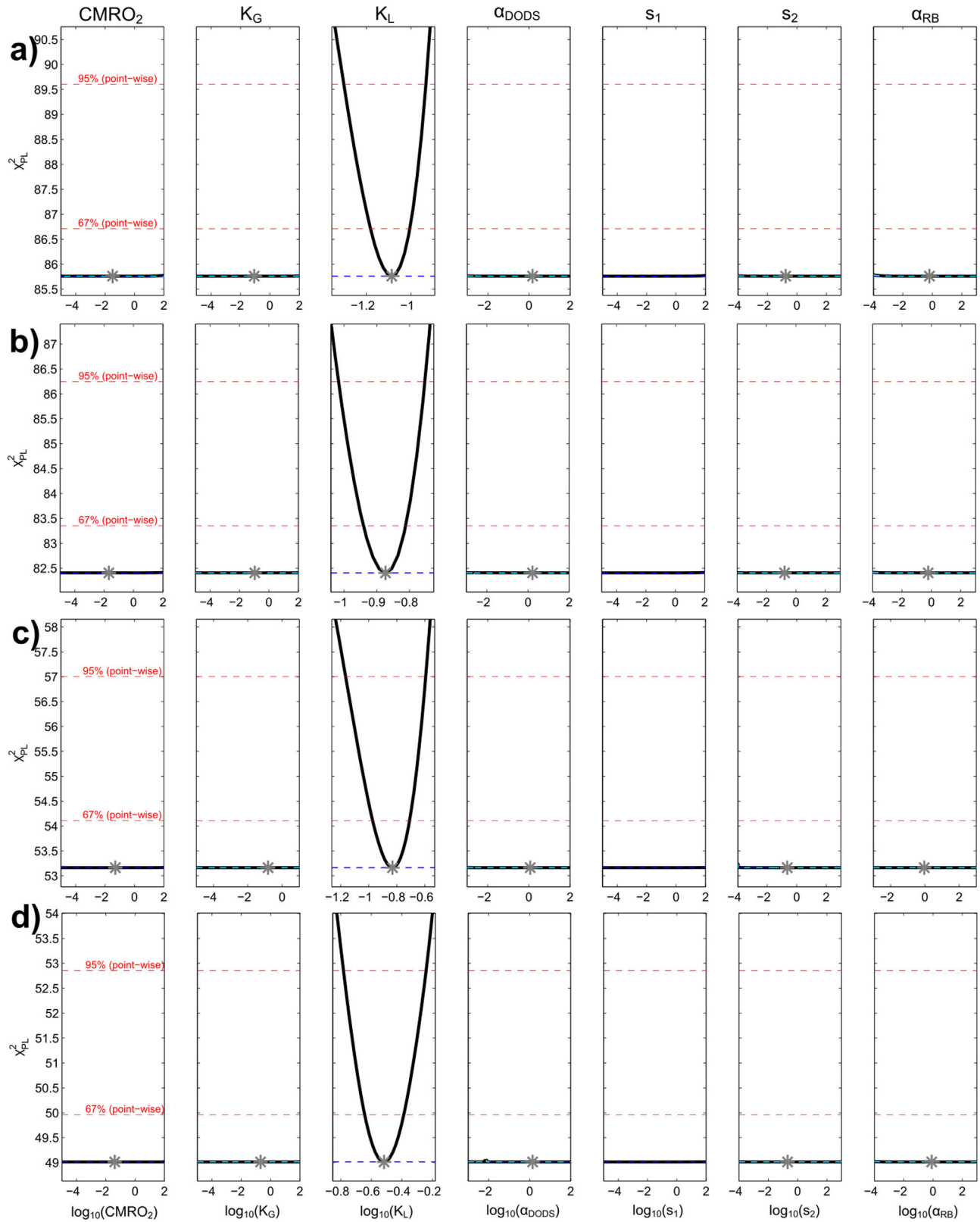
FIG. 3. Exploiting the PL of the parameters of the advanced $CMRO_2$ quantification model in WM (**a, c**) and GM (**b, d**) regions from Exp1 (a, b) and Exp2 (c, d). All presented model parameters were set with a flat prior in log-space (i.e., no prior knowledge about the ^{17}O enrichment fraction α was assumed). Optimal parameter values $\hat{\theta}$ are indicated by asterisks, with the likelihood value indicated by blue lines; thresholds for 95% and 67% CIs are indicated by red dashed lines. Flat CIs indicate structurally non-identifiable parameters. $CMRO_2$, K_G, and K_L have units of $\mu mol/g_{tissue}/min$, $s_1 - min^{-1}$, and $s_2 - min^{-1}$; α_{DODS} and α_{RB} are dimensionless.
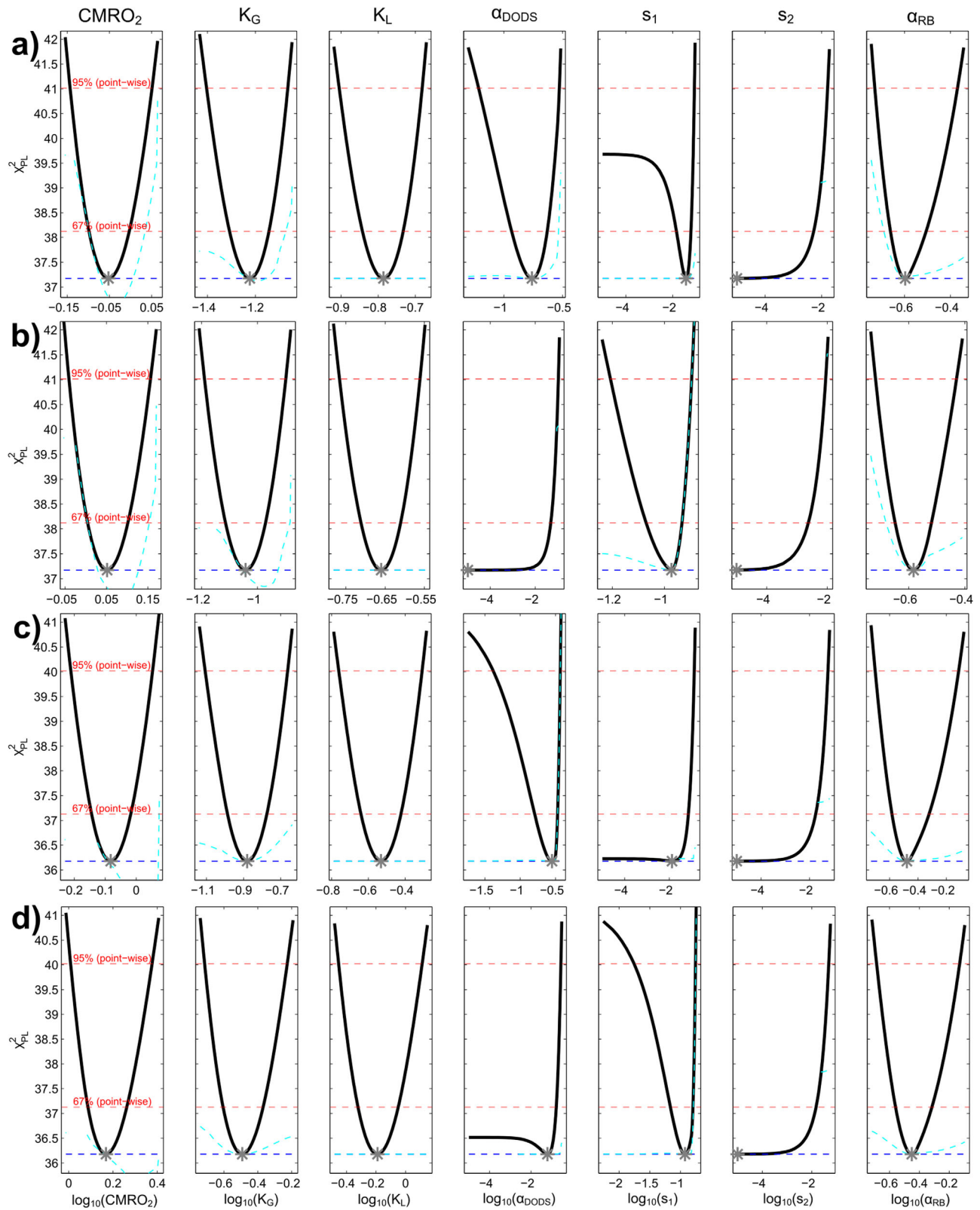
FIG. 4. Exploiting the PL of the parameters of the advanced CMRO$_2$ quantification model in WM (**a, c**) and GM (**b, d**) regions from Exp1 (a, b) and Exp2 (c, d). The averaged α value during the DODS phase was implemented as prior knowledge. Optimal parameter values $\hat{\theta}$ are indicated by asterisks, with the likelihood value indicated by blue lines; thresholds for 95% and 67% CIs are indicated by red dashed lines. Cyan dashed lines represent the contribution of the chosen prior to the respective parameter profile. CMRO$_2$, K_G, and K_L have units of μmol/g$_{tissue}$/min, $s_1 - min^{-1}$, and $s_2 - min^{-1}$; α_{DODS} and α_{RB} are dimensionless.
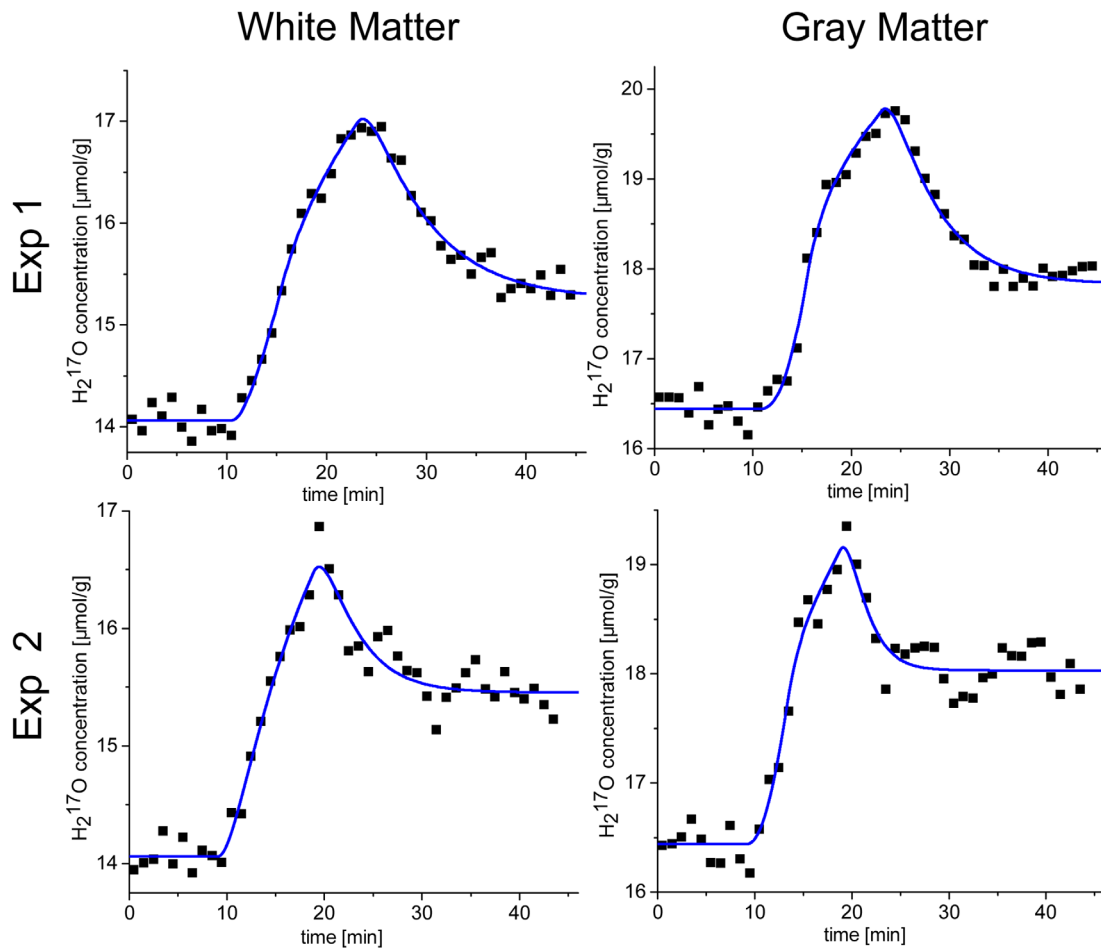
White Matter

Gray Matter

FIG. 5. $H_2{}^{17}O$ signal-time curves obtained in two ^{17}O MR experiments (Exp1 and Exp2) with $^{17}O_2$ gas inhalation in the WM and GM brain regions (black squares). Data fit with the advanced pharmacokinetic model is represented by blue lines. For all data, additional information on the ^{17}O enrichment fraction was taken into account.

The PL is an established method to assess parameter uncertainties in nonlinear settings (39,41,54), where asymptotic CIs based on, for example, Fisher information are typically inappropriate (41). The latter are exact if the solution of the model is linear in the parameters and are a good approximation for a large amount of data and low measurement noise. If these conditions are not fulfilled, the Fisher information is underestimating the true CI and cannot capture the nonlinearity effects outside the region near the optimum. In the ^{17}O MRI experiments, the SNR of the acquired MR images was SNR = 4–6, leading to a relatively high measurement noise. Because the $CMRO_2$ quantification model is nonlinear, asymptotic CIs, which are commonly used in the least-square fitting algorithms, might be misleading.

Initially, the RB system was proposed in (27), where a potential ^{17}O signal during RB phase was excluded from the data analysis due to complexity of the analytical solution of Equation [7]. Later, it was solved for constant α values (33); in this study, a numerical integration was used instead of solving the ODEs analytically. This numerical solution is beneficial for modeling of $H_2{}^{17}O$ signal-time curves because it is more flexible and can be used for more elaborate ^{17}O MRI experiments that, for example, use a lower amount of the rare $^{17}O_2$ gas.

Both the DODS and the RB circuit were used to efficiently deliver and use the rare and costly ^{17}O gas. Decreasing the amount of the ^{17}O gas required for a single patient experiment would directly reduce the total cost of ^{17}O MR examination, which might be an important aspect for clinical studies. The DODS is triggered internally by the patient's inhalation and efficiently delivers a precise and well-defined amount of ^{17}O gas for each inhalation. As originally discussed by Hoffmann

Table 1

Comparison of the $CMRO_2$ Rates in WM and GM Regions of Human Brain (in $\mu mol/g_{tissue}/min$), Quantified with Direct ^{17}O MRI in Two Experiments (Exp1 and Exp2) with $^{17}O_2$ Gas Inhalation, to the Results from ^{15}O-PET (16) and ^{17}O MRI (26,27) Studies

	Exp1	Exp2	^{15}O-PET (16)	^{17}O MRI at 9.4T (26)	^{17}O MRI at 7T (27)
White matter	0.80–0.99	0.72–0.95	0.52–0.72	0.64–0.86	0.50–0.89
Gray matter	1.02–1.27	1.21–1.78	1.36–1.82	1.37–1.47	0.80–1.61

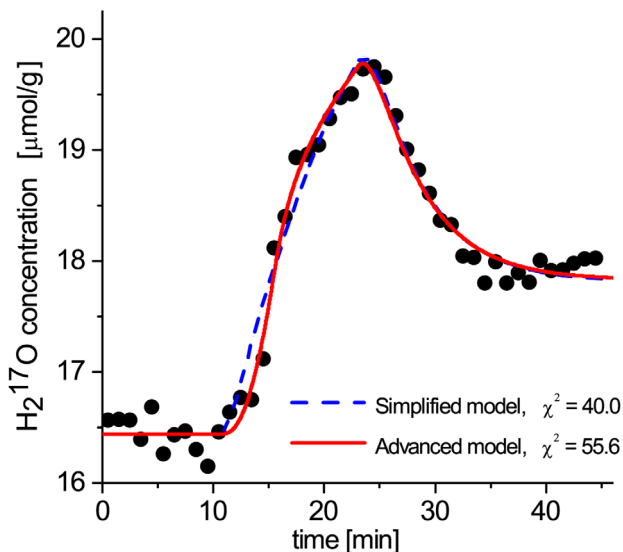FIG. 6. $H_2^{17}O$ signal-time curve obtained in the ^{17}O MR experiment (Exp1) in the GM region (black circles). Data points are fitted with the simplified model with constant α values (dashed blue line) and the advanced CMRO₂ quantification model (red line). Additional information on the ^{17}O enrichment fraction was taken into account.

et al. (27), the risk of gas leakage and accidents in gas handling are minimized, because no transfer of the rare gas from the cylinder is required and standard, clinically approved breathing components can be used. The PL analysis showed that only one α-related parameter needs to be estimated in more complex CMRO₂ quantification model for the MR examination with DODS and RB phases, as it is the case for the experiment with RB phase only (26). The parameters of the advanced model, s_1 and s_2, are practically nonidentifiable but have no influence on either precision or uncertainty of the target parameter CMRO₂.

In this study, the advanced pharmacokinetic model for CMRO₂ quantification was used, which accounts for linearly varying enrichment fraction of the inhaled ^{17}O gas (Fig. 1b). If all model parameters were initialized without prior information, the values of CMRO₂ and α were non-identifiable (Fig. 3). Additional prior information about α_{DODS}, which represents the ^{17}O enrichment from a DODS pulse, was not sufficient to quantify CMRO₂. However, if the averaged α during the DODS phase was taken as prior, the structural non-identifiability of CMRO₂ was resolved (Fig. 4). The identifiability is achieved because both α_{DODS}, which describes the inhaled portion of ^{17}O gas from a fresh DODS pulse, and s_1, which describes the additional amount of ^{17}O gas from the RB circuit, are constrained. This leads to an improved description of the nonlinear increase of $M^{H_2^{17}O}(t)$ through the change from a constant α to a more realistic input shape. In particular, the influence of the $H_2^{17}O$ gain via metabolism and diffusion from blood, which are both positive in Equation [7], can be distinguished by the model and lead to a better description of the data. From an analysis of the parameter profiles, s_2 could be excluded from the model without affecting either the optima or the CIs of the other model parameters. A constant α value during the RB phase is equivalent to a closed RB system in which $^{17}O_2$ gas is homogeneously distributed after the DODS phase and in which the ^{17}O fraction remains constant, although the total amount of oxygen decreases after each inhalation.

As can be seen in Figure 4, either α_{DODS} or s_1 are practically non-identifiable; however, this non-identifiability does not affect the identifiability of the target parameter CMRO₂ and the other model parameters. If s_1 is set to zero, the practical non-identifiability of α_{DODS} is resolved. However, this simplified pharmacokinetic model with constant α values, which has been used previously (27,32,33), led to a significant decrease of χ^2 of the model up to 28% (Fig. 6), whereas CI and optimal values of CMRO₂ were underestimated up to 9%. Thus, the use of the advanced model is beneficial even if not all model parameters can be fully identified.

In the simulation of different uncertainties for the prior information contained in α, a quadratic
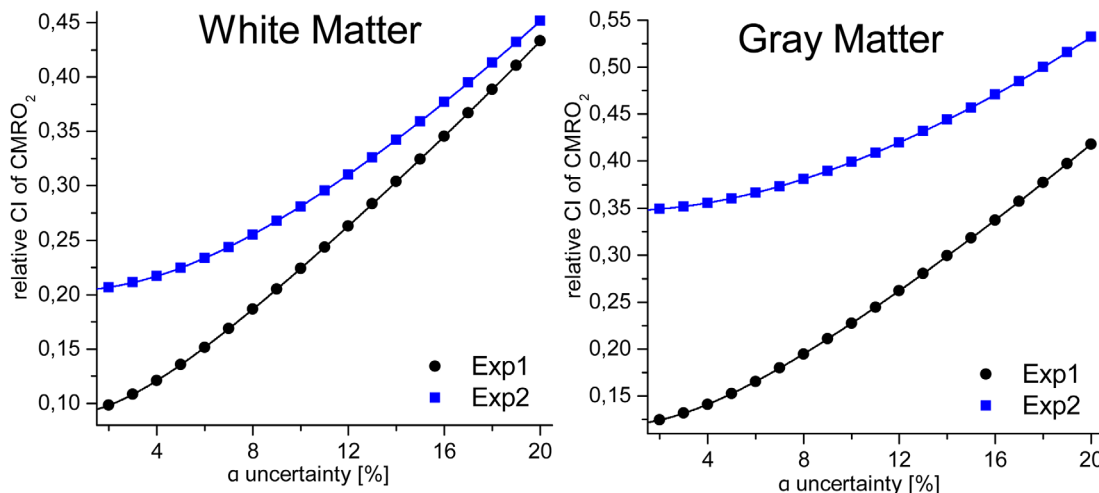

FIG. 7. Relative CIs of CMRO₂ as a function of the uncertainty of the estimated averaged ^{17}O enrichment fraction during the DODS phase (α) for WM (left) and GM (right) brain regions. Calculated values are fitted with a quadratic polynomial for two MR experiments (Exp1 and Exp2).

dependency between the relative CI of $CMRO_2$ and the uncertainty of α could be retrieved, as shown in Figure 7. Precision of α can be increased by measuring the tidal volume and the dead volume of the lungs. The tidal volume can be measured with spirometry, which is a standard pulmonary function test. In addition, when the CO_2 concentration of the exhaled air is measured, the dead space can be calculated. The increase of the α precision from 10% to 5% would lead to an increase in $CMRO_2$ precision of 20%–39%/10%–33% for WM/GM regions.

Another model parameter that affects the $CMRO_2$ value is the arrival time of the first $^{17}O_2$ gas pulse at the alveoli. The $^{17}O_2$ gas bottle and the DODS system, neither of which are MR safe, were placed outside the MR magnet room, and the tube delivering $^{17}O_2$ gas into nasal cannula had a dead volume of 94 mL. Thus, the first two DODS pulses (volume: 40/50 mL in Exp1/Exp2) had a lower $^{17}O_2$ concentration than the remaining pulses due to mixing with the dead volume. In a worst-case scenario, this would lead to 7%–8% underestimation of $CMRO_2$. In our experiments, the DODS system was tested with $^{17}O_2$ gas pulses before the actual MR examination, so that the tube was well filled with $^{17}O_2$ gas. Thus, this time delay potentially only affected the first $^{17}O_2$ pulse, which would lead to a systematic error in the $CMRO_2$ quantification of no more than 1%–2%, which is much smaller than the calculated CIs.

$CMRO_2$ rates obtained in both ^{17}O MRI experiments are in a good agreement with previously reported results of ^{15}O-PET studies (10,13,14,16) and ^{17}O MRI at UHFs (26,27,32,33). Yet, $CMRO_2$ values of GM and WM regions are closer to each other compared with the results of ^{15}O-PET studies (Table 1). This is mainly caused by partial volume effects due to the low spatial resolution of ^{17}O MR images ($\Delta x = 10/8$ mm for Exp1/Exp2) and fast transverse relaxation time $T_2^* = 2$ ms. It increases the theoretical full width of half maximum of the point spread function (55) to 23%; an additional increase of 31% is caused by the radial acquisition of k-space. Thus, almost every pixel of ^{17}O images contains constitutes of several brain regions. The effect of this blurring of the $CMRO_2$ values is lower in Exp2 compared with Exp1, because the nominal spatial resolution of Exp2 was 20% higher. To overcome this limitation, a partial volume correction can be applied using, for example, a "geometric transfer matrix" algorithm as used by Hoffmann et al. (32). Another alternative is to use prior information from the co-registered ^1H images of higher spatial resolution in the iterative reconstruction of ^{17}O MR images, which can be used for partial volume correction (31,56).

The $CMRO_2$ values obtained in ^{17}O MR experiments at UHFs (Table 1) were also affected by partial volume effects. At 9.4T, $CMRO_2$ of 0.64–0.86/1.37–1.47 $\mu mol/g_{tissue}/min$ in WM/GM were found (26). At 7T, $CMRO_2$ values of 0.50–0.89/0.80–1.61 $\mu mol/g_{tissue}/min$ in WM/GM were determined (27), and the values had a higher uncertainty because data from the RB phase needed to be discarded, and an estimation of α needed to be provided. Pixel-wise $CMRO_2$ quantification is the ultimate goal of ^{17}O MR studies but thus far has been obtained only at 9.4T (26). In this preliminary work at 3T, the SNR of the individual dynamic ^{17}O MR images obtained in 1-min

intervals was not sufficient for pixel-wise $CMRO_2$ quantification. To increase SNR, an optimized ^{17}O quadrature coil is under construction and iterative image reconstruction using the mutual information from coregistered ^1H images [e.g., tissues boundaries (31,56)] can be used.

In contrast to models used previously (26,27,33), profile likelihood allows addressing the amount of prior knowledge needed for robust $CMRO_2$ quantification. As shown by the structural identifiability in Figure 3, an arbitrary value of $CMRO_2$ may be determined if no sufficient amount and quality of data are available or if the chosen model renders the parameter non-identifiable. Whenever a nonlinear model is used, the method of profile likelihood should be used to assess accurate uncertainties of the parameters. The practical advantage of the advanced model is the flexibility it gives for ^{17}O MR experiments. Because the model equations do not need to be solved analytically, more efficient and sophisticated ^{17}O gas handling can be modeled, as was the case for the DODS in this study. For example, in future improvements of the setup, the problem of the oxygen shortage at the end of the RB phase will be solved by switching to a ^{16}O gas supply during the RB phase, which can be included in the advanced quantification model. Thus, the volume of ^{16}O gas pulses can be adjusted to compensate for the losses in the RB circuit. In this case, α will significantly decrease and α_{RB} can be calculated based on the amount of the supplied ^{16}O gas.

In general, the profile likelihood approach might also be of interest to investigate identifiability of model parameters in other fields of MRI, as e.g. in dynamic MRI examinations with contrast agent injections, or it could help in other medical imaging techniques, like PET, where tracer kinetics are modeled to determine physiological parameters. In conclusion, the results of the profile likelihood analysis show that $CMRO_2$ can be measured reliably in ^{17}O MRI experiment with ^{17}O gas inhalation if the ^{17}O enrichment fraction is estimated based on the experimental system and introduced as prior information into the model calculations.

REFERENCES

1. Beal MF. Does impairment of energy metabolism result in excitotoxic neuronal death in neurodegenerative illnesses? Ann Neurol 1992;31: 119–130.
2. Frackowiak RSJ, Herold S, Petty RKH, Morgan-Hughes JK. The cerebral metabolism of glucose and oxygen measured with positron tomography in patients with mitochondrial diseases. Brain 1988;111: 1009–1024.
3. Fukuyama H, Ogawa M, Yamauchi H, Yamaguchi S, Kimura J, Yonekura Y, Konishi J. Altered cerebral energy metabolism in Alzheimer's disease: a PET study. J Nucl Med 1994;35:1–6.
4. Ishii K, Kitagaki H, Kono M, Mori E. Decreased medial temporal oxygen metabolism in Alzheimer' s disease shown by PET. J Nucl Med 1996;37:1159–1165.
5. Maurer I, Zierz S, Möller H-J. A selective defect of cytochrome c oxidase is present in brain of Alzheimer disease patients. Neurobiol Aging 2000;21:455–462.
6. Maurer I, Zierz S, Möller H-J. Evidence for a mitochondrial oxidative phosphorylation defect in brains from patients with schizophrenia. Schizophr Res 2001;48:125–136.
7. Wallace DC. Mitochondrial genetics: a paradigm for aging and degenerative diseases? Science 1992;256:628–632.
8. Wallace DC. Mitochondrial diseases in man and mouse. Science 1999;283:1482–1488.

9. Wong-Riley M, Antuono P, Ho KC, Egan R, Hevner R, Liebl W, Huang Z, Rachel R, Jones J. Cytochrome oxidase in Alzheimer's disease: biochemical, histochemical, and immunohistochemical analyses of the visual and other systems. Vision Res 1997;37:3593–3608.

10. Ito M, Lammertsma AA, Wise RJS, Bernardi S, Frackowiak RSJ, Heather JD, McKenzie CG, Thomas DGT, Jones T. Measurement of regional cerebral blood flow and oxygen utilisation in patients with cerebral tumours using ^{15}O and positron emission tomography: analytical techniques and preliminary results. Neuroradiology 1982;23:63–74.

11. Thulborn KR, Davis D, Adams H, Gindin T, Zhou J. Quantitative tissue sodium concentration mapping of the growth of focal cerebral tumors with sodium magnetic resonance imaging. Magn Reson Med 1999;41:351–359.

12. Tyler JL, Diksic M, Villemure JG, Evans AC, Meyer E, Yamamoto YL, Feindel W. Metabolic and hemodynamic evaluation of gliomas using positron emission tomography. J Nucl Med 1987;28:1123–1133.

13. Rhodes CG, Wise RJS, Gibbs JM, Frackowiak RSJ, Hatazawa J, Palmer AJ, Thomas DGT, Jones T. In vivo disturbance of the oxidative metabolism of glucose in human cerebral gliomas. Ann Neurol 1983;14:614–626.

14. Mineura K, Yasuda T, Kowada M, Shishido F, Ogawa T, Uemura K. Positron emission tomographic evaluation of histological malignancy in gliomas using oxygen-15 and fluorine-18-fluorodeoxyglucose. J Neurol Res 1986;8:164–168.

15. Lehnert W, Gregoire M-C, Reilhac A, Meikle SR. Characterisation of partial volume effect and region-based correction in small animal positron emission tomography (PET) of the rat brain. Neuroimage 2012;60:2144–2157.

16. Leenders KL, Perani D, Lammertsma AA, et al. Cerebral blood flow, blood volume and oxygen utilization. Normal values and effect of age. Brain 1990;113:27–47.

17. Mintun MA, Raichle ME, Martin WRW, Herscovitch P. Brain oxygen utilization measured with O-15 radiotracers and positron emission tomography. J Nucl Med 1984;25:177–187.

18. Ter-Pogossian MM, Eichling JO, Davis DO, Welch MJ. The measure in vivo of regional cerebral oxygen utilization by means of oxyhemoglobin labeled with radioactive oxygen-15. J Clin Invest 1970;49:381–391.

19. Mellon EA, Beesam RS, Elliott MA, Reddy R. Mapping of cerebral oxidative metabolism with MRI. Proc Natl Acad Sci USA 2010;107:11787–11792.

20. Hopkins AL, Barr RG. Oxygen-17 compounds as potential NMR T$_2$ contrast agents: enrichment effects of H$_2$^{17}O on protein solutions and living tissues. Magn Reson Med 1987;4:399–403.

21. Regatte RR, Akella SVS, Borthakur A, Reddy R. Proton spin-lock ratio imaging for quantitation of glycosaminoglycans in articular cartilage. J Magn Reson Imaging 2003;17:114–121.

22. Reddy R, Stolpen AH, Leigh JS. Detection of ^{17}O by proton T$_{1rho}$ dispersion imaging. J Magn Reson 1995;108:276–279.

23. Charagundla SR, Stolpen AH, Leigh JS, Reddy R. Off-resonance proton T$_{1rho}$ dispersion imaging of ^{17}O-enriched tissue phantoms. Magn Reson Med 1998;39:588–595.

24. Ronen I, Merkle H, Ugurbil K, Navon G. Imaging of H$_2$^{17}O distribution in the brain of a live rat by using proton-detected ^{17}O MRI. Proc Natl Acad Sci USA 1998;95:12934–12939.

25. Ronen I, Lee J-H, Merkle H, Ugurbil K, Navon G. Imaging H$_2$^{17}O distribution in a phantom and measurement of metabolically produced H$_2$^{17}O in live mice by proton NMR. NMR Biomed 1997;10:333–340.

26. Atkinson IC, Thulborn KR. Feasibility of mapping the tissue mass corrected bioscale of cerebral metabolic rate of oxygen consumption using 17-oxygen and 23-sodium MR imaging in a human brain at 9.4 T. Neuroimage 2010;51:723–733.

27. Hoffmann SH, Begovatz P, Nagel AM, Umathum R, Schommer K, Bachert P, Bock M. A measurement setup for direct ^{17}O MRI at 7 T. Magn Reson Med 2011;66:1109–1115.

28. Zhu X-H, Chen W. In vivo oxygen-17 NMR for imaging brain oxygen metabolism at high field. Prog Nucl Magn Reson Spectrosc 2011;59:319–335.

29. Zhang N, Zhu X-H, Lei H, Ugurbil K, Chen W. Simplified methods for calculating cerebral metabolic rate of oxygen based on ^{17}O magnetic resonance spectroscopic imaging measurement during a short ^{17}O$_2$ inhalation. J Cereb Blood Flow Metab 2004;24:840–848.

30. Borowiak R, Kurzhunov D, Wagner P, Reisert M, Bock M. Dynamic ^{17}O-MRI at 3 Tesla for in vivo CMRO$_2$ quantification. In Proceedings of the 23rd Annual Meeting of ISMRM, Toronto, Canada, 2015. p. 4633.

31. Kurzhunov D, Borowiak R, Wagner P, Reisert M, Bock M. Proton-Constrained CMRO$_2$ Quantification with Direct ^{17}O-MRI at 3 Tesla. In Proceedings of the 23rd Annual Meeting of ISMRM, Toronto, Canada, 2015. p. 2450.

32. Hoffmann SH, Radbruch A, Bock M, Semmler W, Nagel AM. Direct ^{17}O MRI with partial volume correction: first experiences in a glioblastoma patient. MAGMA 2014;27:579–587.

33. Hoffmann SH. Localized quantification of the cerebral metabolic rate of oxygen consumption CMRO$_2$ with ^{17}O magnetic resonance tomography. Heidelberg, Germany: University of Heidelberg; 2011:157.

34. Lu M, Zhang Y, Ugurbil K, Chen W, Zhu X-H. In vitro and in vivo studies of ^{17}O NMR sensitivity at 9.4 and 16.4 T. Magn Reson Med 2013;69:1523–1527.

35. Zhu X-H, Chen JM, Tu T-W, Chen W, Song S-K. Simultaneous and noninvasive imaging of cerebral oxygen metabolic rate, blood flow and oxygen extraction fraction in stroke mice. Neuroimage 2013;64:437–447.

36. Zhu X-H, Zhang Y, Tian R-X, Lei H, Zhang N, Zhang X, Merkle H, Ugurbil K, Chen W. Development of ^{17}O NMR approach for fast imaging of cerebral metabolic rate of oxygen in rat brain at high field. Proc Natl Acad Sci USA 2002;99:13194–13199.

37. Borowiak R, Groebner J, Haas M, Hennig J, Bock M. Direct cerebral and cardiac ^{17}O-MRI at 3 Tesla: initial results at natural abundance. MAGMA 2014;27:95–99.

38. Raue A, Steiert B, Schelker M, et al. Data2Dynamics: a modeling environment tailored to parameter estimation in dynamical systems. Bioinformatics 2015;31:3558–3560.

39. Raue A, Schilling M, Bachmann J, et al. Lessons learned from quantitative dynamical modeling in systems biology. PLoS One 2013;8:e74335.

40. Gudbjartsson H, Patz S. The Rician distribution of noisy MRI data. Magn Reson Med 1995;34:910–914.

41. Raue A, Kreutz C, Maiwald T, Bachmann J, Schilling M, Klingmüller U, Timmer J. Structural and practical identifiability analysis of partially observed dynamical models by exploiting the profile likelihood. Bioinformatics 2009;25:1923–1929.

42. Venzon DZ, Moolgavkar SH. A method for computing profile-likelihood-based confidence intervals. Appl Stat 1988;37:87–94.

43. Neyman J, Pearson ES. On the problem of the most efficient tests of statistical hypotheses. Philos Trans R Soc A Math Phys Eng Sci 1933;231:289–337.

44. Wilks SS. The large-sample distribution of the likelihood ratio for testing composite hypotheses. Ann Math Stat 1938;9:60–62.

45. Nagel AM, Laun FB, Weber M-A, Matthies C, Semmler W, Schad LR. Sodium MRI using a density-adapted 3D radial acquisition technique. Magn Reson Med 2009;62:1565–1573.

46. Jackson JI, Meyer CH, Nishimura DG, Macovski A. Selection of a convolution function for fourier inversion using gridding. IEEE Trans Med Imaging 1991;10:473–478.

47. Ashburner J, Friston KJ. Voxel-based morphometry—the methods. Neuroimage 2000;11:805–821.

48. Ashburner J, Friston KJ. Unified segmentation. Neuroimage 2005;26:839–851.

49. Zhu X-H, Merkle H, Kwag JH, Ugurbil K, Chen W. ^{17}O relaxation time and NMR sensitivity of cerebral water and their field dependence. Magn Reson Med 2001;45:543–549.

50. Whittall KP, MacKay AL, Graeb DA, Nugent RA, Li DKB, Paty DW. In vivo measurement of T$_2$ distributions and water contents in normal human brain. Magn Reson Med 1997;37:34–43.

51. Takagi H, Shapiro K, Marmarou A, Wisoff H. Microgravimetric analysis of human brain tissue: correlation with computerized tomography scanning. J Neurosurg 1981;54:797–801.

52. Coleman TF, Li Y. An interior, trust region approach for nonlinear minimization subject to bounds. SIAM J Optim 1996;6:418–445.

53. Hindmarsh AC, Brown PN, Grant KE, Lee SL, Serban R, Shumaker DE, Woodward CS. SUNDIALS: suite of nonlinear and differential/algebraic equation solvers. ACM Trans Math Softw 2005;31:363–396.

54. Becker V, Schilling M, Bachmann J, Baumann U, Raue A, Maiwald T, Timmer J, Klingmüller U. Covering a broad dynamic range: information processing at the erythropoietin receptor. Science 2010;328:1404–1408.

55. Rahmer J, Börnert P, Groen J, Bos C. Three-dimensional radial ultrashort echo-time imaging with T$_2$ adapted sampling. Magn Reson Med 2006;55:1075–1082.

56. Gnahm C, Bock M, Bachert P, Semmler W, Behl NGR, Nagel AM. Iterative 3D projection reconstruction of ^{23}Na data with an ^{1}H MRI constraint. Magn Reson Med 2014;71:1720–1732.